arXiv:1402.2342v1 [astro-ph.SR] 11 Feb 2014

A MONITORING CAMPAIGN FOR LUHMAN 16AB. I. DETECTION OF RESOLVED NEAR-INFRARED SPECTROSCOPIC VARIABILITY

Adam J. Burgasser[1], Michaël Gillon[2], Jacqueline K. Faherty[3,4], Jacqueline Radigan[5], Amaury H. M. J. Triaud[6,7], Peter Plavchan[8], Rachel Street[9], E. Jehin[2], L. Delrez[2], & C. Opitom[2]

ABSTRACT

We report resolved near-infrared spectroscopic monitoring of the nearby L dwarf/T dwarf binary WISE J104915.57−531906.1AB (Luhman 16AB), as part of a broader campaign to characterize the spectral energy distribution and temporal variability of this system. A continuous 45-minute sequence of low-resolution IRTF/SpeX data spanning 0.8–2.4 μm were obtained, concurrent with combined-light optical photometry with ESO/TRAPPIST. Our spectral observations confirm the flux reversal of this binary, and we detect a wavelength-dependent decline in the relative spectral fluxes of the two components coincident with a decline in the combined-light optical brightness of the system over the course of the observation. These data are successfully modeled as a combination of achromatic (brightness) and chromatic (color) variability in the T0.5 Luhman 16B, consistent with variations in overall cloud opacity; and no significant variability in L7.5 Luhman 16A, consistent with recent resolved photometric monitoring. We estimate a peak-to-peak amplitude of 13.5% at 1.25 μm over the full lightcurve. Using a simple two-spot brightness temperature model for Luhman 16B, we infer an average cold covering fraction of $\approx$30–55%, varying by 15–30% over a rotation period assuming a $\approx$200–400 K difference between hot and cold regions. We interpret these variations as changes in the covering fraction of a high cloud deck and corresponding "holes" which expose deeper, hotter cloud layers, although other physical interpretations are possible. A Rhines scale interpretation for the size of the variable features explains an apparent correlation between period and amplitude for Luhman 16B and the variable T dwarfs SIMP 0136+0933 and 2MASS J2139+0220, and predicts relatively fast winds (1–3 km s^{-1}) for Luhman 16B consistent with lightcurve evolution on an advective time scale (1–3 rotation periods). The strong variability observed in this flux reversal brown dwarf pair supports the model of a patchy disruption of the mineral cloud layer as a universal feature of the L dwarf/T dwarf transition.

Subject headings: binaries: visual — stars: individual (WISE J104915.57−531906.1AB, Luhman 16AB) — stars: low mass, brown dwarfs

1. INTRODUCTION

The driving mechanism for the transition between the L dwarf and T dwarf spectral classes has emerged as one of the outstanding problems in brown dwarf astrophysics. Spectroscopically, this transition is defined by the appearance of CH_4 absorption features at near-infrared wavelengths (Kirkpatrick et al. 1999; Burgasser et al. 2006a), accompanied by a substantial reduction of condensate cloud opacity (Marley et al. 1996;

[1] Center for Astrophysics and Space Science, University of California San Diego, La Jolla, CA 92093, USA; aburgasser@ucsd.edu
[2] Institute of Astrophysics and Géophysique, Université of Liège, allée du 6 Août, 17, B-4000 Liège, Belgium
[3] Department of Terrestrial Magnetism, Carnegie Institution of Washington, 5241 Broad Branch Road NW, Washington, DC 20015, USA
[4] Hubble Fellow
[5] Space Telescope Science Institute, 3700 San Martin Drive, Baltimore, MD 21218, USA
[6] Massachusetts Institute of Technology, Kavli Institute for Astrophysics and Space Research, 77 Massachusetts Avenue, Cambridge, MA 02139, USA
[7] Fellow of the Swiss National Science Foundation
[8] NASA Exoplanet Science Institute, California Institute of Technology, M/C 100-22, 770 South Wilson Avenue, Pasadena, CA 91125, USA
[9] LCOGT, 6740 Cortona Drive, Suite 102, Goleta, CA 93117, USA

Burrows et al. 2000; Allard et al. 2001). Both effects drive near-infrared spectral energy distributions (SEDs) to transition from red ($J − K \approx 1.5 − 2.5$) to blue ($J − K \approx 0 − 0.5$; Leggett et al. 2000; Marley et al. 2002; Burgasser et al. 2006a), with strengthening molecular gas bands delineating the spectral subclasses. What is remarkable about the L dwarf/T dwarf transition is that it appears to take place over a relatively narrow range of effective temperatures (T_{eff}s) and luminosities, based on absolute magnitude trends (e.g., Dahn et al. 2002; Vrba et al. 2004), broad-band SED measurements (e.g., Golimowski et al. 2004) and spectral model fits (e.g., Cushing et al. 2008; Stephens et al. 2009). The L/T transition also exhibits an apparent excess of binaries (Burgasser 2007), gaps in color distributions (Dupuy & Liu 2012) and a decline in number densities as a function of spectral type (Metchev et al. 2008), trends that suggest the transition is rapid in time as well as temperature.

The important role of photospheric cloud evolution for this transition is seen in the observation that early-type T dwarfs with minimal cloud opacity are often significantly brighter at 1 μm than their hotter, cloudier L dwarf counterparts. This is true in both color-magnitude diagrams of local populations (Tinney et al. 2003; Faherty et al. 2012; Dupuy & Liu 2012) and among components of "flux-reversal" binaries that straddle the L/T transition

(Burgasser et al. 2006b; Liu et al. 2006; Looper et al. 2008). The 1 μm region is a minimum of molecular gas opacity—the local pseudocontinuum—so condensate grain scattering can dominate the overall opacity at these wavelengths (Ackerman & Marley 2001). The 1 μm brightening has thus been interpreted as a depletion of photospheric condensate clouds over a narrow range of T_{eff} and/or time. The geometry of the depletion has been modeled as both global changes in photospheric chemistry (e.g., Knapp et al. 2004; Tsuji 2005; Burrows et al. 2006; Saumon & Marley 2008) and hole formation that allows light to emerge from hotter regions (Ackerman & Marley 2001; Burgasser et al. 2002; Marley et al. 2010). The latter hypothesis predicts an enhancement of rotationally-modulated photometric variability at the L/T transition, particularly in the 1 μm region, depending on the sizes and distribution of the cloud gaps.

Recent brown dwarf monitoring observations support this prediction, as the two most prominent variables identified to date, SIMP J013656.5+093347 (Artigau et al. 2006, 2009; hereafter SIMP J0136+0933) and 2MASS J21392676+0220226 (Reid et al. 2008; Radigan et al. 2012; hereafter 2MASS J2139+0220) are both early-type T dwarfs. Their variability can be reproduced with spot models assuming regions with thick and thin clouds at different temperatures assumed to probe different layers in the atmosphere (Radigan et al. 2012; Apai et al. 2013). The spectral character of the observed variability is nevertheless complex. Rather than variability being limited to pseudocontinuum regions where gas opacity is a minimum, broad-band chromatic and achromatic variations are seen across the infrared (Artigau et al. 2009; Radigan et al. 2012). The light curve shapes themselves are also seen to change over several rotation periods, suggesting dynamic evolution of features at rates considerably faster than the Solar gas giants (Showman & Kaspi 2013). Finally, variability measurements over widely-separated spectral regions have recently revealed evidence of pressure-dependent phase variations, indicating vertical structure in the features driving the variability (Buenzli et al. 2012; Biller et al. 2013). The considerable level of detail on brown dwarf cloud structure and atmospheric dynamics garnered from these monitoring studies is of relevance to exoplanet atmospheres, where clouds are now seen as a key opacity source (Barman et al. 2011; Madhusudhan et al. 2011; Marley et al. 2012; Pont et al. 2013; Crossfield et al. 2013).

The recently-discovered, nearby binary brown dwarf system WISE J104915.57−531906.1AB (hereafter Luhman 16AB; Luhman 2013) has emerged as a potential benchmark for studying the L/T transition. With spectral types of L7.5 and T0.5 (Kniazev et al. 2013; Burgasser et al. 2013), its components straddle the transition. Its T dwarf secondary is brighter than the primary in the 0.95–1.3 μm range, making it a flux-reversal system (Burgasser et al. 2013). Luhman 16AB is also a significant variable. Combined-light red optical photometry by Gillon et al. (2013) revealed peak-to-peak variability of $\sim$10% with a period of 4.87±0.01 hr, with large changes in the light curve structure over daily timescales. The variability was attributed primarily to the T dwarf component. Resolved photometry by Biller et al. (2013)

extended the observed variability into the near-infrared, confirmed Luhman 16B as the dominant variable, and revealed pressure-dependent phase variations. As such, this system embodies nearly all of the remarkable characteristics of the L/T transition—multiplicity, variability, and flux reversal—while residing only 2.020±0.019 pc from the Sun (Boffin et al. 2013).

In April 2013, our consortium organized a week-long monitoring campaign of Luhman 16AB using telescopes in Chile, Australia and Hawaii, with the aim of characterizing its variability panchromatically (radio, optical and infrared) and spectroscopically, while simultaneously obtaining kinematic data (radial and rotational velocities) to constrain its orbit and viewing geometry. This article reports low-resolution near-infrared spectroscopic monitoring observations obtained over 45 minutes with the SpeX spectrometer (Rayner et al. 2003) on the 3.0m NASA Infrared Telescope Facility (IRTF), coincident with combined-light optical photometry obtained with the TRAnsiting Planets and PlanetesImals Small Telescope (TRAPPIST; Jehin et al. 2011). In Section 2 we describe our observation and data reduction procedures, including period analysis of the TRAPPIST lightcurve around this epoch. In Section 3 we describe our spectral extraction and variability analysis of the SpeX data, and create an empirical model to replicate both the SpeX and TRAPPIST observations. In Section 4 we discuss our results, examining the nature of Luhman 16B's inferred variability in the context of a simple two-spot brightness temperature model, and compare this source to other significantly variable L/T transition objects. We summarize our results in Section 5.

2. OBSERVATIONS

2.1. *IRTF/SpeX Spectroscopy*

Luhman 16AB was observed with IRTF/SpeX on 26 April 2013 (UT) in clear and dry conditions with variable seeing. We used the 0$\farcs$5 slit and prism-dispersed mode to obtain $\lambda/\Delta\lambda \approx 120$ spectra covering 0.7–2.5 μm. The source was monitored for just over an hour, between UT times 06:05 and 07:10, while seeing ranged from 0$\farcs$8 to >2$''$. The slit was aligned along the binary axis at a position angle of 313° (east of north) to obtain simultaneous spectroscopy; note that this differed significantly from the parallactic angle of Luhman 16AB, which varied from 12° through 0° and back to 4° during the sequence. We obtained 70 exposures of 30 s each in an ABBA dither pattern. The source never exceeded an elevation of 17° above the horizon, and the airmass ranged from a maximum of 3.565 to a minimum of 3.420 at UT 06:51, then back up to 3.438 at the end of the sequence. The choice of a narrow slit was driven by guiding considerations, which was done on spill-over light from the primary using the $H+K$ notch filter.[10] For calibration, we observed the A0 V star HD 87760 ($V = 7.89$) prior to the monitoring run at an airmass of 3.277 and with the slit aligned to the same (non-parallactic) position angle. Internal flat field and Ar arc lamp exposures were obtained for pixel response and wavelength calibration.

We performed an initial extraction of the combined-

---

[10] This filter spans 1.47–2.4 μm with a transmission notch at 1.8 μm to block out the telluric H_2O absorption band; see http://www.ifa.hawaii.edu/$\sim$tokunaga/filterSpecs.html.

light spectrum as described in Burgasser et al. (2013), using SpeXtool (Vacca et al. 2003; Cushing et al. 2004) with standard settings but a wide spatial aperture that encompassed both sources. This coarse extraction provided the wavelength calibration, telluric correction and relative flux calibration files necessary for subsequent component extractions. The combined light spectrum is slightly redder $(\Delta(J-K) = 0.1)$ than that reported in Burgasser et al. (2013), which may reflect slit losses from differential color refraction or intrinsic variability. Detailed extraction of the component spectra are described below.

2.2. *TRAPPIST Imaging*

Throughout the overall campaign, Luhman 16AB was monitored with TRAPPIST, a 0.6 m robotic telescope located at La Silla Observatory in Chile. The telescope is equipped with a thermoelectrically-cooled 2K×2K CCD camera with a 0″.65 pixel scale and a 22′×22′ field of view. The camera images through a broad-band I + z filter with >90% transmission from 0.75—1.1μm, the long-wavelength cutoff set by the quantum efficiency of the CCD detector. Luhman 16AB was observed for roughly 7.5 hr on 26 April 2013 (UT). Data were reduced as described in Gillon et al. (2013). After a standard pre-reduction (bias, dark, flatfield correction), aperture photometry was performed using IRAF/DAOPHOT2 (Stetson 1987) with an aperture radius of 8 pixels (5″.2) that encompassed both sources. Differential photometry was determined by comparison to a grid of non-varying background stars, and the resulting light curve normalized.

That light curve is shown in Figure 1. As in the original detection, Luhman 16AB exhibits significant variability over the observing period with a peak-to-peak amplitude of 5% in a roughly sinusoidal pattern. To determine the variability period, we used the phase dispersion minimization technique (Stellingwerf 1978), cycling through 500 periods linearly spaced between 7.0 min (5 times the minimum sampling) and 7.1 hr (80% of the full observational period). For each period, we phase-folded the light-curve, computed a mean curve sampled at 50 phase points across the period, then computed the χ^2 deviation of the phased data from the mean curve. We performed the same analysis with the data randomly shuffled 100 times to compute a baseline deviation (χ^2_{sh}). Figure 1 shows that ratio of these deviations as a function of period, $\Theta = \chi^2(p)/\chi^2_{sh}$, which exhibits a broad minimum[11] at 5.05±0.10 hr, longer than but statistically consistent (1.8σ) with the period measurement of Gillon et al. (2013). The phased lightcurve repeats over the 1.5 periods observed, consistent with rotationally-modulated surface structure.

3. SPECTRAL VARIABILITY ANALYSIS

3.1. *Extraction of Component Spectra*

Given the seeing conditions during our SpeX observations, the component spectra are blended to varying degrees at all wavelengths. In order to robustly separate the

[11] The uncertainty of the best-fit period was determined by computing the uncertainty in Θ at each period by varying the photometric data about the measurement uncertainties 100 times. The range of periods for which Θ is within 1σ of the minimum value set the period uncertainty.
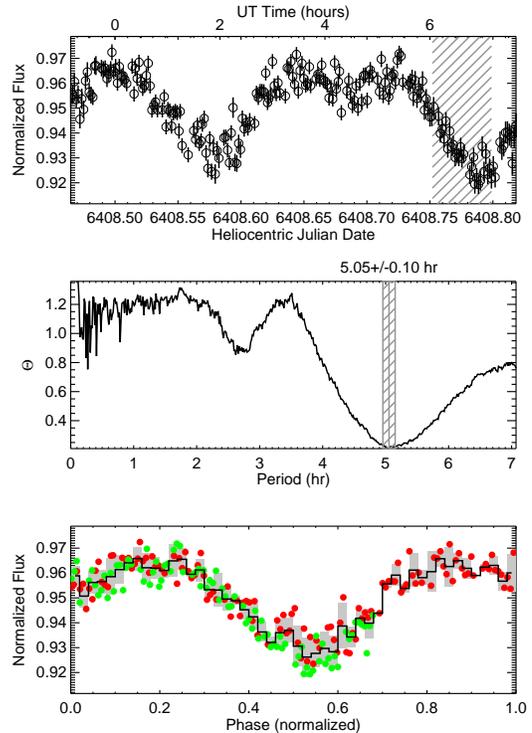

FIG. 1.— (Top) TRAPPIST light-curve for the combined system of Luhman 16AB on 26 April 2013 (UT). Flux values have been normalized to a global maximum. The cross-hatched region indicates the period during which SpeX data were obtained. (Middle) Phase-dispersion deviation statistic $\Theta \equiv \chi^2(p)/\chi^2_{sh}$ for TRAPPIST data phase folded over period p. A broad minimum is found at 5.05±0.10 hr, the uncertainty determined by randomly sampling the measurement uncertainties. (Bottom) Phase-folded light curve at 5.05 hr, with the two cycles observed indicated as red and green points. The black histogram traces the mean light curve sampled at 50 phase points, while the grey bars indicate the 1σ scatter of the datapoints at that phase.

spectra, we directly modeled the individual data frames. We first pairwise-subtracted the raw frames, dividing each by the median-combined flat-field frame generated by SpeXtool, and then excised 48-pixel (7″.2) regions from each image along the spatial direction that encompassed both component spectral traces. For these subimages, we performed a column-by-column fit of the spatial profiles with a six-component gaussian model: a central gaussian and two satellites for each component, with the satellites constrained to have the same separations and relative peaks for both components. All gaussians were forced to have the same widths to reduce parameter degeneracies, and each three-gaussian component profile was allowed to vary independently in amplitude and position. Including a constant background value, this 10-parameter model was initialized by fitting to an integrated profile (summing all columns corresponding to wavelengths 1.0–1.3 μm, 1.55–1.75 μm and 2.05–2.3 μm) and then fitting each column individually starting from the integrated profile parameters. The fits were converged using an implementation of the Nelder-Mead simplex algorithm (AMOEBA; Nelder 1965; Press et al. 1986) to minimize the reduced chi-square statistic,

$$\chi^2_r = \frac{1}{N_{UM} - 10} \sum_i W_i \frac{(P_i - M_i)^2}{\sigma_i^2}, \qquad (1)$$

between the spatial profile P and model M, scaled by the image variance σ^2. A masking vector W was determined by repeating the fit three times and excluding highly deviant pixels ($>3\sigma$), resulting in N_{UM} unmasked pixels in a given column. Component fluxes at each image column were integrated directly from the final profile model, and flux uncertainties (σ_λ) were determined as

$$\sigma_\lambda^2 = N_{eff}\langle\sigma^2\rangle\chi_r^2 = \frac{\sum_i M_i}{\max(\{M\})}\langle\sigma^2\rangle\chi_r^2 \qquad (2)$$

where N_{eff} is the effective number of pixels used to determine the flux based on the model, and $\langle\sigma^2\rangle$ is the standard deviation between model and image counts for unmasked pixels in the spatial profile. This combination is multiplied by χ_r^2 to account for systematic deviations in the profile model.

Figures 2 and 3 illustrate the quality of these fits, comparing the observed and modeled profiles as well as data and model images. When the observed seeing was below 1″2 (which encompassed 49 images in the period 6:03–6:46 UT), the profile fits converged exceptionally well, with fit residuals and corresponding spectral uncertainties typically 0.5-1% in the brightest spectral regions. The modeling was also generally resistant to bad pixels, with the exception of a spectral detector crack visible in the 2.36–2.40 μm region in Figure 2.

Visually apparent even in the raw data, our observations confirm the flux reversal between Luhman 16A and B reported by Burgasser et al. (2013). As shown in Figure 3, the T dwarf component is on average 20% brighter at Y and J and 20% fainter at K compared to the L dwarf component. Figure 4 displays these differences across the full spectral range, showing that Luhman 16B is the brighter component from 0.95-1.33 μm, and marginally brighter even from 1.55–1.65 μm. Again, these are the spectral regions that are most influenced by condensate grain scattering and absorption in the L dwarfs, indicating that cloud opacity plays a primary role in the observed flux reversal.

3.2. Relative Spectral Light Curves

The observed fluxes are affected by three systematic effects: (1) slit losses due to the finite slit width used, which will vary with seeing and telescope tracking; (2) changes in atmospheric transmission due to the changing airmass over the observation; and (3) differential color refraction (DCR) induced by observing the pair aligned along their binary axis rather than the parallactic angle. The last two factors are particularly problematic for this observation given the large airmass at which Luhman 16AB was observed. Rather than devise a model to compensate for these effects, potentially introducing new systematic errors, we focused our analysis on relative flux variations over narrow spectral bands. This choice mitigates slit loss and transmission variations which affect both sources equally, and we assume that DCR does not induce significant color variation over a sufficiently narrow wavelength range.[12]

We quantified variability by measuring the relative observed fluxes of the two components, $R(\lambda,t) =$

$F_B(\lambda,t)/F_A(\lambda,t)$, in 0.03 μm bands ($\approx$2–3 resolution elements) between 0.9–2.3 μm (Figure 4). We used the χ^2 statistic to assess the presence of variability for each spectral band over the observing period:

$$\chi^2(\lambda) = \sum_{i=1}^{N_{obs}}\frac{(R(\lambda,t_i) - R_{\mathrm{model}}(\lambda,t_i))^2}{\sigma^2(\lambda,t_i)}. \qquad (3)$$

Here, $N_{obs} = 49$, $\sigma(t)$ is the uncertainty in relative flux at time t_i (typically 1–3%) and $R_{\mathrm{model}}(\lambda,t)$ is the modeled value. We considered the two simplest models of constant flux ($R_{\mathrm{model}}(\lambda,t) = R_0(\lambda)$) and linear variation with time ($R_{\mathrm{model}} = R_0(\lambda) + \alpha(\lambda)t$), and found that the latter was a statistically significant better fit to the timeseries data in the pseudocontinuum regions based on the F-test statistic (confidence of 95% or greater). Figure 4 displays the linear slopes in percentage change per hour as a function of wavelength. Nearly all of the regions for which time variability is statistically significant are those in which Luhman 16B is the brighter component and, assuming identical radii, has a higher brightness temperature[13] (T_{br}). This result is consistent with the results of Gillon et al. (2013) and Biller et al. (2013), who find that Luhman 16B dominates the observed variability of the system. The magnitude of $\alpha(\lambda)$ decreases with increasing wavelength, from 10% hr^{-1} at 1 μm to 4% hr^{-1} at 2.1 μm. This is qualitatively similar to broad-band photometric variations of SIPS J0136+0933 (Artigau et al. 2009) and 2MASS J2139+0220 (Radigan et al. 2012), which are observed to be greater at J than K. On the other hand, the sense of this variation is also consistent with the declining brightness of Luhman 16B relative to the seemingly invariable Luhman 16A (Biller et al. 2013). We also note small declines in $\alpha(\lambda)$ in regions of strong H$_2$O absorption (1.35–1.45 μm, 1.8–2.0 μm), although signals-to-noise in these regions are much lower.

We show the time series of the relative fluxes in significantly variable bands and in broader spectral regions (0.1 μm) encompassing the Y (1.12–1.22 μm), J (1.25–1.35 μm), H (1.6–1.7 μm), and K (2.1–2.2 μm) flux peaks in Figure 4. Remarkably, all of these regions show a common morphology: a fast ($\sim$3 min) dimming of order 5% at UT 6:08, followed by a much slower decline for the remainder of the observing period. The fast dimming does not appear to be related to sudden changes in seeing or airmass; indeed, a step-up in seeing at 6:24 UT does not coincide with any feature in the light curves. We verified that the decline beyond 6:08 remained significant for three regions in the J-band (1.095 μm, 1.125 μm and 1.215 μm) where Luhman 16B is brightest, with a linear declining trend of 5–6% hr^{-1}. Examining the broad-band

---

[12] Because these observations were taken at large zenith angle (18° off the horizon), we cannot implicitly assume DCR effects are negligible in the near-infrared; see Stone (1996).

[13] To compute T$_{br}$ values, we first determined the scaling term for Luhman 16A that converts its apparent spectral flux to surface flux based on its measured absolute J-band magnitude of 15.00±0.04 (Burgasser et al. 2013; Boffin et al. 2013) and a radius of 0.86±0.06 R$_{Jupiter}$ using the evolutionary models of Burrows et al. (2001) and assuming T$_{eff}$ ≈ 1300–1500 K and an age of 1-5 Gyr. We applied the same scaling to Luhman 16B. Brightness temperatures were assigned by determining the Planck blackbody that provides an equivalent flux density. The absolute brightness temperature values have uncertainties of 4% based on uncertainties in the absolute magnitudes and radii of the sources, but relative temperature differences between the two components are certain to better than 0.5%.
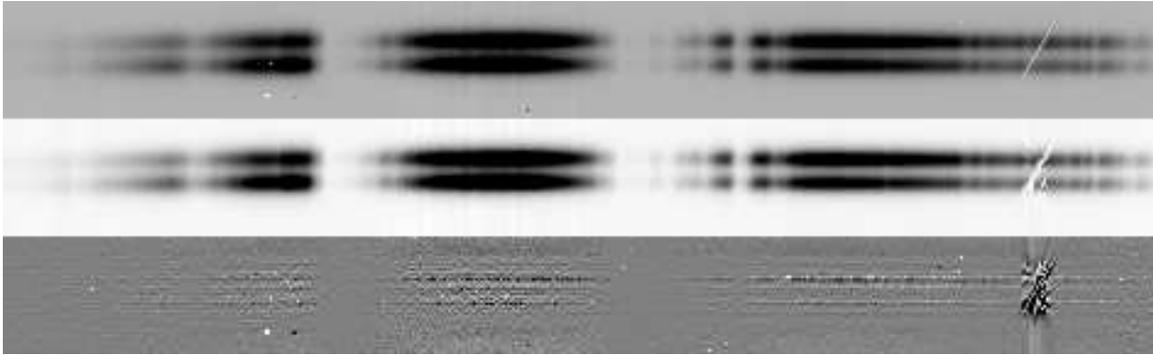
FIG. 2.— Illustration of the forward-modeling extraction of one spectral data frame. The top panel displays the pair-wise subtracted and flat-fielded data frame at UT time 06:02:36. The middle panel displays the model data frame generated from the profile-fitting described in the text. The bottom panel shows the residual image, with contrast scaled up by a factor of 10 compared to the other two frames.
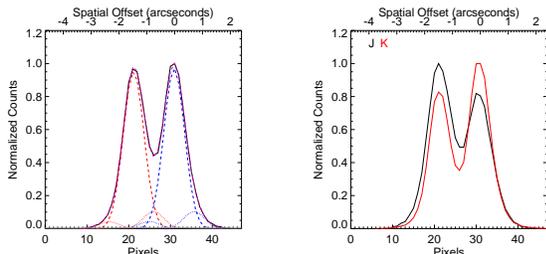

FIG. 3.— (Left): Normalized spatial profile from the image in Figure 2 integrated over wavelengths 1.0–1.3 μm, 1.55–1.75 μm and 2.05–2.3 μm (black) compared to model profile (purple) with gaussian sub-components for primary (red) and secondary (blue) shown. The profile uncertainties (grey) are <1% and undetectable on this plot. (Right): Comparison of normalized spatial profiles at J-band (black; 1.0–1.3 μm) and K-band (red; 2.05–2.3 μm), illustrating the flux reversal between the components.

spectral peak relative fluxes, we again see a wavelength dependence during the slow decline, with F_B/F_A changing the most at Y and J bands and the least at K. Overall, it appears that the relative fluxes of these two components underwent a sharp then gradual decrease over the observing period, amounting to a $\approx$7.5% ($\approx$5%) decline in brightness at J (K) over 45 min. Note that our limited time coverage prevents assessment of the $\sim$100° phase difference between J and K variations reported by Biller et al. (2013).

The decline in relative spectral fluxes aligns well with a decline in combined red optical light as measured by TRAPPIST (hatched region in Figure 1). The spectral monitoring period coincided with a 2.5% decrease in total brightness, or a 4% hr^{-1} linear trend with time, shallower than our near-infrared spectral band measurements. Since a decline in relative flux must be caused by a dimming secondary and/or brightening primary, and a decline in total flux by a dimming secondary and/or dimming primary, we logically conclude from both of these datasets that Luhman 16B is the variable component, in agreement with Gillon et al. (2013) and Biller et al. (2013).

3.3. An Empirical Model of the Observed Spectral Variability

If Luhman 16B is the primary variable in this system, the wavelength dependence of the observed spectral variations, particularly in the pseudocontinuum regions where they are significant, arises from three possible effects. First, achromatic changes in the pseudocon-

tinuum caused by pulsation and/or achromatic opacity variations, that manifest as a wavelength-dependent variation due to the changing relative fluxes of the two components across the near-infrared; second, chromatic variations arising from changes in intrinsically wavelength-dependent opacities; and third, a combination of both. To assess the underlying nature of Luhman 16B's variability, we used a simple empirical model to replicate both SpeX and TRAPPIST observations during the monitoring period. Assuming Luhman 16A was invariable in the near-infrared during the time of our observations (<0.3% variability was reported by Biller et al. 2013 in 4 hr of observation), and that the variability of Luhman 16B is linear (or nearly so) in time and/or wavelength over the period observed, the simplest model for the spectrum of Luhman 16B taking into account these effects is:

$$F_B(\lambda, t) = F_{B,0}(\lambda) \times [a_0 + a_1(t-t_0) + a_2(\lambda-\lambda_0) + a_3(t-t_0)(\lambda-\lambda_0)]. \quad (4)$$

Here, $F_{B,0}(\lambda)$ is the median spectrum of Luhman 16B over the monitoring period, t_0 is the start of the period, $\lambda_0 = 1.77$ μm is the median wavelength of the spectrum, and the parameters a_0, a_1, a_2 and a_3 are linear coefficients taking into account relative scaling, achromatic time variation, chromatic scaling and chromatic time variation, respectively. Assuming $F_A(\lambda, t) = F_{A,0}(\lambda)$, we used this function to calculate the linear rate of change of the relative spectra ($\alpha(\lambda)$), as well as the combined light of the system integrated over a constant 0.75–1.1 μm passband to simulate the TRAPPIST data.

Applying the Nelder-Mead algorithm with a χ^2 evaluation, we determined the best parameters for Equation 4 fitting only for $\alpha(\lambda)$. We also performed fits in which one or more parameters were forced to be zero to assess their significance. The best-fit model, shown in Figure 4, required all terms except a_2, with $a_0 = 1.39$, $a_1 = -0.0549$ hr^{-1} and $a_3 = 0.0468$ hr^{-1} μm^{-1}. Fitting with a_2 gave similar values for the other parameters but made the overall fit slightly worse. Excluding either the achromatic (a_1) or chromatic (a_3) variation terms, or both, produced significantly worse fits which could be excluded at >95% confidence based on the F-test statistic.

We may therefore conclude that both achromatic and chromatic pseudocontinuum variations were present in Luhman 16B during the monitoring period, variations that are consistent with changes in the cloud covering fraction (Ackerman & Marley 2001). The positive value
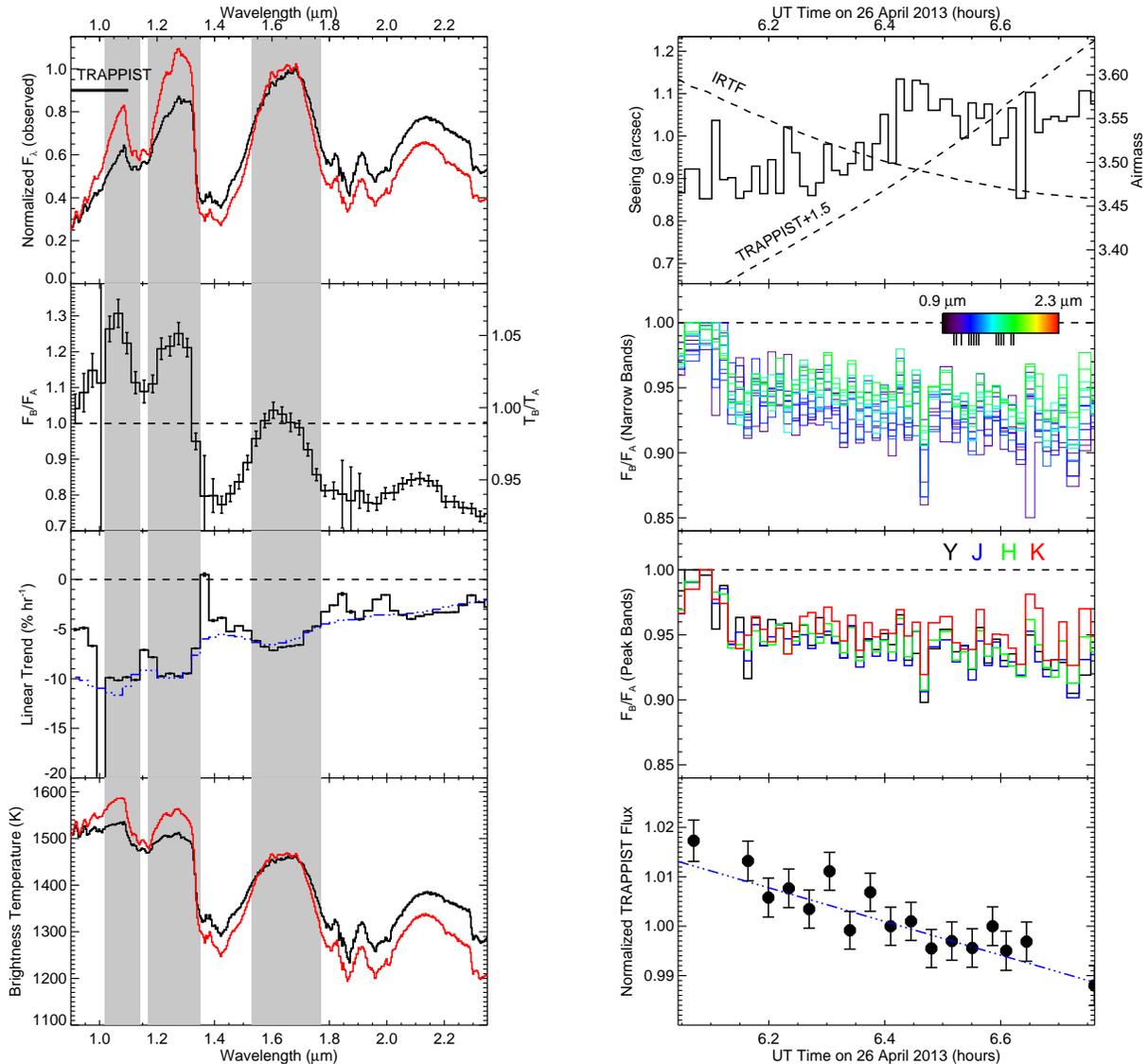
FIG. 4.— Variability analysis from spectral (left) and temporal (right) perspectives. (Left Top): Observed fluxes for Luhman 16A (black) and B (red), averaged over the observing period and normalized by a common factor. The TRAPPIST passband is indicated. (Left 2nd): Relative fluxes (F_B/F_A) averaged over the observing period, with error bars indicating the range of measured values. (Left 3rd): Inferred linear variations of relative fluxes as a function of wavelength during the observing period. The blue line represents the best empirical model fit. (Left Bottom): Brightness temperature spectra for Luhman 16A (black) and B (red). In all panels the shaded regions indicate spectral regions with statistically significant variability based on the F-test. (Right Top): Seeing for IRTF observations (black solid line, left axis) and airmass for IRTF and TRAPPIST observations (black dashed line, right axis) during the monitoring period. (Right 2nd): Time variation of F_B/F_A in narrow spectral bands (0.03 μm) with statistically significant variability. (Right 3rd): Same as above but for broader band (0.1 μm) $YJHK$ peak fluxes. (Right Bottom): TRAPPIST light curve over the same period, with the best-fit empirical model shown in blue.

of a_3 is particularly relevant here, as it indicates that the variable opacity source plays a greater role at shorter wavelengths where gas opacity is minimal, as expected if that source is condensate grain opacity. The predicted TRAPPIST light curve for the model constrained by the SpeX spectra also agrees well with that data (Figure 4). In particular, the model produces a smaller amplitude of optical variation due to the reduced contribution of Luhman 16B to the combined light of the system at these wavelengths.

4. DISCUSSION

4.1. Interpreting the Nature of Luhman 16B's Spectral Variability

Spectral trends in variability have been examined in several L and T dwarfs to date, through pure spectroscopy (e.g., Bailer-Jones 2008; Goldman et al. 2008; Apai et al. 2013) and simultaneous or near-simultaneous broad-band imaging (e.g., Koen et al. 2004; Artigau et al. 2009; Buenzli et al. 2012; Radigan et al. 2012; Khandrika et al. 2013; Heinze et al. 2013; Biller et al. 2013). The most significant variables up until now, SIMP J0136+0933 and 2MASS J2139−0220, both exhibit color trends in near-infrared photometric variability, with larger ampli-

tude changes at J as compared to K, again consistent with variable condensate cloud opacity. However, spectroscopic variability measurements of these same two sources over 1.0–1.7 μm by Apai et al. (2013) indicate that achromatic or near-achromatic variations dominate the psuedocontinuum. These authors propose a two-layer cloud model with a thick shallow cloud and thin deep cloud as a means of reproducing both achromatic psuedocontinuum and chromatic broadband variability. Matched to atmosphere models, this framework can replicate observed trends in the colors and spectral shapes of SIMP J0136+0933 and 2MASS J2139−0220 over 1-3 rotation periods, although detailed fits to the data remain poor (see also Radigan et al. 2012).

For Luhman 16B, we also find that both achromatic and chromatic variations must be present in the psuedo-continuum to properly model the observations. Achromatic variation yields a decline in the overall flux, amounting to roughly 0.03 mag in broad-band J over the observing period. The concurrent chromatic variation simultaneously reddens the spectrum of this source by $\Delta(J - K) = 0.02$ mag, resulting in a relative flux variation amplitude of $\Delta F_{K_s}/\Delta F_J = 0.41\pm0.18$, similar to values reported for SIMP J0136+0933 (Artigau et al. 2009) and 2MASS J2139−0220 (Radigan et al. 2012). Combined, the achromatic and chromatic terms nearly cancel in the K-band, a region that is gas opacity dominated (H_2O, CH_4 and H_2). Hence, our linear spectral model is functionally consistent with condensate clouds being the primary driver of variability in Luhman 16B.

4.2. A Brightness Temperature Spot Model for Luhman 16B

Given the known shortcomings in reproducing the near-infrared spectra of L/T transition brown dwarfs (e.g., Leggett et al. 2008; Cushing et al. 2008; Stephens et al. 2009), we forgo detailed modeling of the spectra in lieu of a simply brightness temperature variation model, focusing at 1.25 μm where gas opacity is a minimum and cloud structure variations are expected to have the greatest influence (Ackerman & Marley 2001). The simplest model for replicating the surface flux $\langle F \rangle$ of a patchy brown dwarf is two sets of regions with differing brightness temperatures covering the surface:

$$\langle F \rangle \propto \langle T_{br}{}^4 \rangle \equiv A T_{cold}^4 + (1 - A)T_{hot}^4. \qquad (5)$$

Here, $\langle T_{br}{}^4 \rangle$ is the disk-averaged brightness temperature, T_{cold} and T_{hot} are the brightness temperatures of cold and hot regions, respectively, $A \equiv F_{cold}/\langle F \rangle \leq 1$ is the areal covering fraction of the cold regions, and we ignore limb darkening. Our interpretation of this model is that the cold regions correspond to the highest cloud layer in the brown dwarf atmosphere, while the hot regions correspond to gaps in these clouds that probe to some as-yet undetermined deeper layer with brightness temperature T_{hot}; a cartoon perspective of this is shown in Figure 6 of Apai et al. (2013). We note that this is not the only interpretation of a two-spot model, which could also arise from magnetic interaction at the photosphere (i.e., starspots) or updrafts of warm air pockets driven by convective flows. Nevertheless, we will occasionally refer to the cold region as "clouds" and hot regions as "holes" in the following discussion.
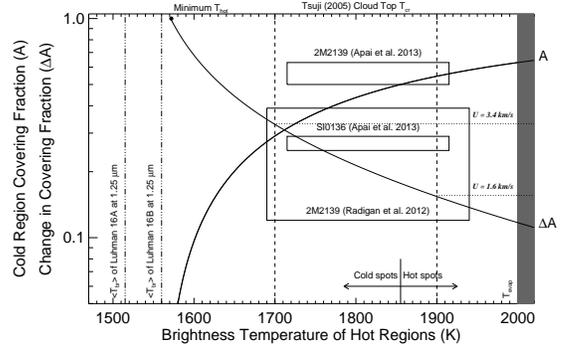
FIG. 5.— Cold spot covering fraction A and change in covering fraction ΔA (solid lines) on Luhman 16B over a full cycle, as a function of the hot spot brightness temperature at 1.25 μm. Values for A are derived from Eqn. 5 and assume $\langle T_{br} \rangle_{L16B} = 1560$ K and $T_{cold} = \langle T_{br} \rangle_{L16A} = 1510$ K, based on Figure 4 (vertical triple-dot dash lines). Values for ΔA are derived from Eqns. 6 and 7 and assume $\Delta F/F = 13.5\%$. The point where $\Delta A = 100\%$ indicates the minimum T_{hot}; the temperature at which $A = 0.5$ is also labeled, separating cold surfaces with hot spots from a hot surface with cold spots. Also labeled are the range of T_{cr} values from Tsuji (2005) and Sorahana & Yamamura (2012) that estimate the height of cloud tops, and the temperature at which all condensates are assumed to be evaporated (T_{evap}). Estimates for A and T_{hot} for SIMP J0136+0933 and 2MASS J2139−0220 from Radigan et al. (2012) and Apai et al. (2013) are indicated, assuming the same cloud top temperature. Finally, we label estimates of jet size scales for wind velocities of $U = 1.6$ km s^{-1} and 3.4 km s^{-1} based on a Rhines length scale (Eqn. 8); these intersect the ΔA curve at $T_{hot} = 1700$ K and 1900 K.

For Luhman 16B, $\langle T_{br} \rangle = 1560$ K at the 1.25 μm J-band peak continuum (Figure 4; see also Faherty et al. 2014). If we take the brightness temperature of Luhman 16A at this wavelength, 1510 K, as an estimate for T_{cold} for both sources,[14] then we can jointly constrain A and T_{hot}, as illustrated in Figure 5. Coverage of cold regions is essentially negligible for $T_{hot} < 1570$ K, then climbs to over 50% at $T_{hot} \approx 1860$ K. At hotter temperatures, our model predicts that the atmosphere of Luhman 16B would be overall similar to that of Luhman 16A with occasional hot spots, which we assume to be less than the evaporation temperature of mineral condensate species ($T_{evap} \approx 2000$ K; Lodders 1999). We note that equal hot-cold spot coverage for Luhman 16B occurs in the 1700–1900 K range that Tsuji (2005) estimate as the effective top of a brown dwarf cloud layer (T_{cr}; see Sorahana & Yamamura 2012). Radigan et al. (2012) and Apai et al. (2013) also provide estimates for A and $\Delta T_{hc} = T_{hot} - T_{cold}$ for SIMP J0136+0933 and 2MASS J2139−0220 based on their own two-spot modeling. While temperature values reported in these studies are based on model effective temperatures, if we assume that the brightness temperature offsets are the same as their preferred $\Delta T_{hc} \approx 300$ K, this would also place the hot regions of Luhman 16B in the same temperature range as the cloud tops of the Tsuji (2005) models. Thus, if our spot model is interpreted as probing different layers of Luhman 16B's atmosphere, the best estimates of the temperature differential is in line with the conjecture of Apai et al. (2013) that gaps in the highest cloud deck still probe regions influenced by condensate opacity.

[14] The assumption can be justified in part by the nearly identical brightness temperatures of the two sources in the 1.15 μm region, where H_2O and CH_4 opacity play a larger role than clouds.

However, we stress that our data cannot independently determine A or T_{hot}, and other interpretations of these temperature differences are conceivable.

The fractional peak-to-peak variation in observed flux that occurs as hot and cold regions rotate in and out of view is

$$\frac{\Delta F}{\langle F \rangle} = \frac{\Delta A}{A - \epsilon} \qquad (6)$$

where $\langle F \rangle$ is the average flux, ΔF the change in total flux, ΔA the change in cloud coverage (increasing A decreases the total flux), and $\epsilon \equiv F_{hot}/(F_{hot} - F_{cold}) = T_{hot}^4/(T_{hot}^4 - T_{cold}^4) \geq 1$; see also Radigan et al. (2012).[15] In terms of brightness temperatures:

$$\Delta T_{br} = \frac{\Delta F}{4\langle F \rangle}\langle T_{br} \rangle = \frac{\Delta A}{4(A - \epsilon)}\langle T_{br} \rangle. \qquad (7)$$

During our observations, we observed a 7.5% variation in the J-band peak continuum that was coincident with a 2.5% variation in TRAPPIST red-optical photometry. We therefore assume that the full 4.5% peak-to-peak variation in TRAPPIST photometry around our spectral observations (Figure 1) corresponds to a 13.5% variation at J, or a peak-to-peak temperature fluctuation of $\Delta T_{br} \approx 50$ K[16] following Eqn 7. This temperature offset is notably similar to the temperature difference between Luhman 16A and B at these wavelengths (Figure 4). Using the relationship between A and T_{hot} above, we computed ΔA as a function of T_{hot}, also shown in Figure 5. Not surprisingly, the areal variation required to reproduce the observed brightness variations declines with higher T_{hot}; i.e., with greater contrast between cold and hot regions. An important reference point is the temperature at which areal variations become smaller than the total cold region coverage, which occurs for $T_{hot} > 1710$ K and $A > 30\%$. The corresponding $\Delta T_{hc} = 150$ K is on the low end of estimates for SIMP J0136+0933 and 2MASS J2139−0220, and just above the minimum T_{cr} from Tsuji (2005). For the range 1700 K $< T_{hot} <$ 1900 K, which we again take as a reasonable estimates of the hot spot temperature, the inferred cold covering fraction is roughly 30–55%, intermediate between similar values inferred for SIMP J0136+0933 (25-30%) and 2MASS J2139−0220 (50-65%) by Apai et al. (2013).

4.3. Interpretation: Rhines Length Scale and Advective Time Scale

For 1700 K $< T_{hot} <$ 1900 K, cold spot coverage must vary by 15–30% over a single period to replicate the observed variability amplitude, implying a $\sim$ 30-100% variation between hemispheres if the spot patterns are static. Organized jet features in the atmospheres of the giant Solar planets generally scale in size with the Rhines length (Rhines 1970; Showman et al. 2008), $L_{Rh} \sim (U/2\Omega R \cos\phi)^{1/2}$, where U the characteristic

wind speed, R is the radius, $\Omega = 2\pi/P$, P is the rotation period and ϕ is the latitude of the feature. If we assume that the same scaling occurs for features in brown dwarf atmospheres (e.g., Apai et al. 2013; Showman & Kaspi 2013), then their maximum fractional size scale is:

$$\alpha_{Rh} \sim \left(\frac{L_{Rh}}{R}\right)^2 \approx 2\% \left(\frac{U}{\text{km/s}}\right)\left(\frac{P}{\text{hr}}\right)\left(\frac{R_{Jup}}{R}\right). \quad (8)$$

where we have assumed mid-latitude features. If we now relate this maximum scale to the areal spot variation inferred here ($\alpha_{Rh} \sim \Delta A$), the known rotational period and assumed radius of Luhman 16B implies characteristic wind speeds of 1.6 km s^{-1} $< U <$ 3.4 km s^{-1} for 1700 K $< T_{hot} <$ 1900 K (Figure 5). These speeds are somewhat higher than the range favored by the circulation models of Showman & Kaspi (2013), assuming winds are driven by inefficient conversion of convective heat (10–300 m s^{-1}). However, the speeds do give advection timescales, $\tau_{adv} \sim R/U \sim (2 - 5) \times 10^4$ s $\sim 1 - 3$ rotation periods, that are consistent with the timescale of lightcurve evolution observed in Luhman 16B (Gillon et al. 2013).

The convergence between the inferred variation and Rhines length scales, and the advective and evolutionary time scales, suggest that our gross estimates for T_{cold}, T_{hot}, A and ΔA are not too far off the mark. However, we have made a number of major assumptions that require confirmation through more detailed spectroscopic monitoring and modeling, in particular to ascertain whether the spot regions have spectral characteristics (features and line profile shapes) consistent with the inferred brightness temperatures. Nonetheless, our basic model of a cold cloud deck disrupted by warm dynamic features shows promising agreement with planetary analogs and current brown dwarf circulation models.

4.4. Trends in L/T Transition Variability

Luhman 16B joins SIMP J0136+0933 and 2MASS J2139−0220 as the three most variable L/T transition objects detected to date, so it is worth comparing the variability properties of these sources, summarized in Table 1. The variability period, J-band variability amplitude and inferred cloud covering fraction of Luhman 16B are all intermediate between those of SIMP J0136+0933 and 2MASS J2139−0220, although epoch-to-epoch changes in these values are considerable. As the Rhines scale scales linearly with the rotation period,[17] its interpretation as an estimate of surface feature size is consistent with Luhman 16B's intermediate period and intermediate variability amplitude, as a few large features are more likely to give rise to stronger disk-integrated variations than many small features (Apai et al. 2013). There also appears to be a correlation between rotation period and cloud covering fraction, although temperature effects may play a role in this statistic. The source with the smallest cloud coverage, SIMP J0136+0933, is also

---

[15] Our expression differs slightly from Radigan et al. (2012) because we assign A to be the cloud-covering fraction, whereas they define the equivalent parameter a as the cloud-cleared fraction.

[16] The maximum variation observed by Gillon et al. (2013) over weeks of monitoring is 10%, which would correspond to 30% variations in J, exceeding those observed in 2MASS J2139−0220. However, we restrict our analysis here to the period around the spectral observations since the spectral response of larger fluctuations may differ.

[17] Apai et al. (2013) incorrectly state a spot scaling law of P^{-2} in the text, but infer a spot scaling between 2MASS J2139−0220 and SIMP J0136+0933 that is consistent with $A \propto P$; the former is likely a typographical error.

TABLE 1
COMPARISON OF HIGHLY VARIABLE L/T TRANSITION DWARFS.

Source	SpT	P_{rot} (hr)	$\Delta F/F$ at 1.25 μm	A	$\Delta K/\Delta J$	Ref
SIMP J0136+0933	T2.5	2.3895±0.0005	5.5%	25-30%	0.48±0.06	1,2
Luhman 16B	T0.5	4.87±0.01	13.5%[a]	30-55%[b]	0.41±0.18	3,4
2MASS J2139−0220	T1.5	7.721±0.005	30%	50-65%	0.45–0.83	2,5

REFERENCES. — (1) Artigau et al. (2009); (2) Apai et al. (2013); (3) Gillon et al. (2013); (4) This paper; (5) Radigan et al. (2012).
[a] Based on the maximum peak-to-peak TRAPPIST variability amplitude during the current observing period.
[b] Assuming $T_{hot} - T_{cold} = 300\pm100$ K; see Apai et al. (2013).

the latest-type and presumably coldest brown dwarf in the sample. Finally, we find essentially no difference in color variability among these sources. As noted above, our estimate of $\Delta F_{K_s}/\Delta F_J$ for Luhman 16B is consistent with similar measures for SIMP J0136+0933 and 2MASS J2139−0220 (although the latter can exhibit more extreme color terms; Radigan et al. 2012), suggesting that the condensate clouds responsible for the variations in these sources are likely to have similar opacities and physical properties (i.e., composition, grain size distribution, vertical structure, etc.). However, confirmation of this agreement will again require more careful spectral modeling to accurately determine cloud properties.

5. SUMMARY

We have measured significant variability in the resolved, relative spectral fluxes of Luhman 16A and B using IRTF/SpeX. Variations occur at all wavelengths, most significantly in the bands where Luhman 16B is the brighter source. We detect both a rapid decline of 5% in about 3 min, and a subsequent slow decline in the remaining 45 min of observation, with rates ranging from -10% hr^{-1} at 1.25 μm to -4% hr^{-1} at 2.1 μm. By comparing to concurrent combined-light photometry from TRAPPIST, we deduce that the observed variability originates from the T0.5 secondary, confirming the results of Gillon et al. (2013) and Biller et al. (2013). We are able to successfully reproduce both the SpeX and TRAPPIST lightcurves with an empirical model that assumes Luhman 16A is constant while Luhman 16B undergoes both achromatic and chromatic pseudocontinuum flux variations. Qualitatively, this model may be interpreted as arising from variations in cloud covering fraction in the photosphere of Luhman 16B as it rotates, although other physical models (starspots, gas upwelling) may also apply. Using a simple two-spot model that assumes cold regions are identical to the atmosphere of Luhman 16A, we are able to deduce an average and variance in the cold (or cloud) covering fraction of Luhman 16B as a function of the temperature of hot (or hole) regions. While the hot region temperature remains a free parameter, a range of 1700–1900 K is supported by the cloud models of Tsuji (2005) and the tem-

perature contrasts inferred for SIMP J0136+0933 and 2MASS J2139−0220. This range is also supported by the supposition that surface features follow a Rhines scale, and predict wind velocities of 1–3 km s^{-1}. These are higher than early expectations from brown dwarf circulation modeling, but consistent with advection timescales that align with lightcurve variability over a few rotation periods. Rhines scale-sized features also explain the apparent trend between variability period and amplitude between SIMP J0136+0933, Luhman 16B and 2MASS J2139−0220.

The relative spectral fluxes of Luhman 16A and B, the presence of significant near-infrared variability on Luhman 16B, and the spectral nature of this variability all align with the model of cloud evolution through fragmentation as a driving mechanism for the L/T transition. However, other physical interpretations remain viable, and the influence of secondary parameters (surface gravity, metallicity, viewing perspective) are only starting to be explored (Metchev & Hillenbrand 2006; Burgasser et al. 2010; Madhusudhan et al. 2011). Given its unique composition and proximity to the Sun, the Luhman 16AB system should continue to be monitored as a benchmark for cloud structure and evolution in cool brown dwarf and exoplanet atmospheres.

Facilities: IRTF: SpeX, TRAPPIST

REFERENCES

Ackerman, A. S., & Marley, M. S. 2001, ApJ, 556, 872

Allard, F., Hauschildt, P. H., Alexander, D. R., Tamanai, A., & Schweitzer, A. 2001, ApJ, 556, 357

Apai, D., Radigan, J., Buenzli, E., Burrows, A., Reid, I. N., &
   Jayawardhana, R. 2013, ApJ, 768, 121
Artigau, É., Bouchard, S., Doyon, R., & Lafrenière, D. 2009, ApJ,
   701, 1534
Artigau, É., Doyon, R., Lafrenière, D., Nadeau, D., Robert, J., &
   Albert, L. 2006, ApJ, 651, L57
Bailer-Jones, C. A. L. 2008, MNRAS, 384, 1145
Barman, T. S., Macintosh, B., Konopacky, Q. M., & Marois, C.
   2011, ApJ, 733, 65
Biller, B. A., Crossfield, I. J. M., Mancini, L., Ciceri, S.,
   Southworth, J., Kopytova, T. G., Bonnefoy, M., Deacon, N. R.,
   Schlieder, J. E., Buenzli, E., Brandner, W., Allard, F.,
   Homeier, D., Freytag, B., Bailer-Jones, C. A. L., Greiner, J.,
   Henning, T., & Goldman, B. 2013, ApJ, 778, L10
Boffin, H. M. J., Pourbaix, D., Muzic, K., Ivanov, V. D., Kurtev,
   R., Beletsky, Y., Mehner, A., Berger, J. P., Girard, J. H., &
   Mawet, D. 2013, ArXiv e-prints
Buenzli, E., Apai, D., Morley, C. V., Flateau, D., Showman,
   A. P., Burrows, A., Marley, M. S., Lewis, N. K., & Reid, I. N.
   2012, ApJ, 760, L31
Burgasser, A. J. 2007, ApJ, 659, 655
Burgasser, A. J., Cruz, K. L., Cushing, M., Gelino, C. R., Looper,
   D. L., Faherty, J. K., Kirkpatrick, J. D., & Reid, I. N. 2010,
   ApJ, 710, 1142
Burgasser, A. J., Geballe, T. R., Leggett, S. K., Kirkpatrick,
   J. D., & Golimowski, D. A. 2006a, ApJ, 637, 1067
Burgasser, A. J., Kirkpatrick, J. D., Cruz, K. L., Reid, I. N.,
   Leggett, S. K., Liebert, J., Burrows, A., & Brown, M. E. 2006b,
   ApJS, 166, 585
Burgasser, A. J., Marley, M. S., Ackerman, A. S., Saumon, D.,
   Lodders, K., Dahn, C. C., Harris, H. C., & Kirkpatrick, J. D.
   2002, ApJ, 571, L151
Burgasser, A. J., Sheppard, S. S., & Luhman, K. L. 2013, ApJ,
   772, 129
Burrows, A., Hubbard, W. B., Lunine, J. I., & Liebert, J. 2001,
   Reviews of Modern Physics, 73, 719
Burrows, A., Marley, M. S., & Sharp, C. M. 2000, ApJ, 531, 438
Burrows, A., Sudarsky, D., & Hubeny, I. 2006, ApJ, 640, 1063
Crossfield, I. J. M., Barman, T., Hansen, B. M. S., & Howard,
   A. W. 2013, A&A, 559, A33
Cushing, M. C., Marley, M. S., Saumon, D., Kelly, B. C., Vacca,
   W. D., Rayner, J. T., Freedman, R. S., Lodders, K., & Roellig,
   T. L. 2008, ApJ, 678, 1372
Cushing, M. C., Vacca, W. D., & Rayner, J. T. 2004, PASP, 116,
   362
Dahn, C. C., Harris, H. C., Vrba, F. J., Guetter, H. H., Canzian,
   B., Henden, A. A., Levine, S. E., Luginbuhl, C. B., Monet,
   A. K. B., Monet, D. G., Pier, J. R., Stone, R. C., Walker,
   R. L., Burgasser, A. J., Gizis, J. E., Kirkpatrick, J. D., Liebert,
   J., & Reid, I. N. 2002, AJ, 124, 1170
Dupuy, T. J., & Liu, M. C. 2012, ApJS, 201, 19
Faherty, J. K., Beletsky, Y., Burgasser, A. J., Tinney, C. G.,
   Osip, D. J., & Simcoe, R. A. 2014, ApJ, submitted
Faherty, J. K., Burgasser, A. J., Walter, F. M., Van der Bliek, N.,
   Shara, M. M., Cruz, K. L., West, A. A., Vrba, F. J., &
   Anglada-Escudé, G. 2012, ApJ, 752, 56
Gillon, M., Triaud, A. H. M. J., Jehin, E., Delrez, L., Opitom, C.,
   Magain, P., Lendl, M., & Queloz, D. 2013, A&A, 555, L5
Goldman, B., Cushing, M. C., Marley, M. S., Artigau, É.,
   Baliyan, K. S., Béjar, V. J. S., Caballero, J. A., Chanover, N.,
   Connelley, M., Doyon, R., Forveille, T., Ganesh, S., Gelino,
   C. R., Hammel, H. B., Holtzman, J., Joshi, S., Joshi, U. C.,
   Leggett, S. K., Liu, M. C., Martín, E. L., Mohan, V., Nadeau,
   D., Sagar, R., & Stephens, D. 2008, A&A, 487, 277
Golimowski, D. A., Leggett, S. K., Marley, M. S., Fan, X.,
   Geballe, T. R., Knapp, G. R., Vrba, F. J., Henden, A. A.,
   Luginbuhl, C. B., Guetter, H. H., Munn, J. A., Canzian, B.,
   Zheng, W., Tsvetanov, Z. I., Chiu, K., Glazebrook, K.,
   Hoversten, E. A., Schneider, D. P., & Brinkmann, J. 2004, AJ,
   127, 3516
Heinze, A. N., Metchev, S., Apai, D., Flateau, D., Kurtev, R.,
   Marley, M., Radigan, J., Burgasser, A. J., Artigau, É., &
   Plavchan, P. 2013, ApJ, 767, 173
Jehin, E., Gillon, M., Queloz, D., Magain, P., Manfroid, J.,
   Chantry, V., Lendl, M., Hutsemékers, D., & Udry, S. 2011, The
   Messenger, 145, 2

Khandrika, H., Burgasser, A. J., Melis, C., Luk, C., Bowsher, E.,
   & Swift, B. 2013, AJ, 145, 71
Kirkpatrick, J. D., Reid, I. N., Liebert, J., Cutri, R. M., Nelson,
   B., Beichman, C. A., Dahn, C. C., Monet, D. G., Gizis, J. E.,
   & Skrutskie, M. F. 1999, ApJ, 519, 802
Knapp, G. R., Leggett, S. K., Fan, X., Marley, M. S., Geballe,
   T. R., Golimowski, D. A., Finkbeiner, D., Gunn, J. E.,
   Hennawi, J., Ivezić, Z., Lupton, R. H., Schlegel, D. J., Strauss,
   M. A., Tsvetanov, Z. I., Chiu, K., Hoversten, E. A.,
   Glazebrook, K., Zheng, W., Hendrickson, M., Williams, C. C.,
   Uomoto, A., Vrba, F. J., Henden, A. A., Luginbuhl, C. B.,
   Guetter, H. H., Munn, J. A., Canzian, B., Schneider, D. P., &
   Brinkmann, J. 2004, AJ, 127, 3553
Kniazev, A. Y., Vaisanen, P., Mužić, K., Mehner, A., Boffin,
   H. M. J., Kurtev, R., Melo, C., Ivanov, V. D., Girard, J.,
   Mawet, D., Schmidtobreick, L., Huelamo, N., Borissova, J.,
   Minniti, D., Ishibashi, K., Potter, S. B., Beletsky, Y., Buckley,
   D. A. H., Crawford, S., Gulbis, A. A. S., Kotze, P., Miszalski,
   B., Pickering, T. E., Romero Colmenero, E., & Williams, T. B.
   2013, ApJ, 770, 124
Koen, C., Matsunaga, N., & Menzies, J. 2004, MNRAS, 354, 466
Leggett, S. K., Geballe, T. R., Fan, X., Schneider, D. P., Gunn,
   J. E., Lupton, R. H., Knapp, G. R., Strauss, M. A., McDaniel,
   A., Golimowski, D. A., Henry, T. J., Peng, E., Tsvetanov, Z. I.,
   Uomoto, A., Zheng, W., Hill, G. J., Ramsey, L. W., Anderson,
   S. F., Annis, J. A., Bahcall, N. A., Brinkmann, J., Chen, B.,
   Csabai, I., Fukugita, M., Hennessy, G. S., Hindsley, R. B.,
   Ivezić, Ž., Lamb, D. Q., Munn, J. A., Pier, J. R., Schlegel,
   D. J., Smith, J. A., Stoughton, C., Thakar, A. R., & York,
   D. G. 2000, ApJ, 536, L35
Leggett, S. K., Saumon, D., Albert, L., Cushing, M. C., Liu,
   M. C., Luhman, K. L., Marley, M. S., Kirkpatrick, J. D.,
   Roellig, T. L., & Allers, K. N. 2008, ApJ, 682, 1256
Liu, M. C., Leggett, S. K., Golimowski, D. A., Chiu, K., Fan, X.,
   Geballe, T. R., Schneider, D. P., & Brinkmann, J. 2006, ApJ,
   647, 1393
Lodders, K. 1999, ApJ, 519, 793
Looper, D. L., Gelino, C. R., Burgasser, A. J., & Kirkpatrick,
   J. D. 2008, ApJ, 685, 1183
Luhman, K. L. 2013, ApJ, 767, L1
Madhusudhan, N., Burrows, A., & Currie, T. 2011, ApJ, 737, 34
Marley, M. S., Saumon, D., Cushing, M., Ackerman, A. S.,
   Fortney, J. J., & Freedman, R. 2012, ApJ, 754, 135
Marley, M. S., Saumon, D., & Goldblatt, C. 2010, ApJ, 723, L117
Marley, M. S., Saumon, D., Guillot, T., Freedman, R. S.,
   Hubbard, W. B., Burrows, A., & Lunine, J. I. 1996, Science,
   272, 1919
Marley, M. S., Seager, S., Saumon, D., Lodders, K., Ackerman,
   A. S., Freedman, R. S., & Fan, X. 2002, ApJ, 568, 335
Metchev, S. A., & Hillenbrand, L. A. 2006, ApJ, 651, 1166
Metchev, S. A., Kirkpatrick, J. D., Berriman, G. B., & Looper, D.
   2008, ApJ, 676, 1281
Nelder, J. A. & Mead, R. 1965, Computer Journal, 7, 308
Pont, F., Sing, D. K., Gibson, N. P., Aigrain, S., Henry, G., &
   Husnoo, N. 2013, MNRAS, 432, 2917
Press, W. H., Flannery, B. P., & Teukolsky, S. A. 1986,
   Numerical recipes. The art of scientific computing
Radigan, J., Jayawardhana, R., Lafrenière, D., Artigau, É.,
   Marley, M., & Saumon, D. 2012, ApJ, 750, 105
Rayner, J. T., Toomey, D. W., Onaka, P. M., Denault, A. J.,
   Stahlberger, W. E., Vacca, W. D., Cushing, M. C., & Wang, S.
   2003, PASP, 115, 362
Reid, I. N., Cruz, K. L., Kirkpatrick, J. D., Allen, P. R., Mungall,
   F., Liebert, J., Lowrance, P., & Sweet, A. 2008, AJ, 136, 1290
Rhines, P. 1970, Geophysical and Astrophysical Fluid Dynamics,
   1, 273
Saumon, D., & Marley, M. S. 2008, ApJ, 689, 1327
Showman, A. P., & Kaspi, Y. 2013, ApJ, 776, 85
Showman, A. P., Menou, K., & Cho, J. 2008, in Astronomical
   Society of the Pacific Conference Series, Vol. 398, Astronomical
   Society of the Pacific Conference Series, ed. D. Fischer,
   F. A. Rasio, S. E. Thorsett, & A. Wolszczan, 419–+
Sorahana, S., & Yamamura, I. 2012, ApJ, 760, 151
Stellingwerf, R. F. 1978, ApJ, 224, 953

Stephens, D. C., Leggett, S. K., Cushing, M. C., Marley, M. S.,
    Saumon, D., Geballe, T. R., Golimowski, D. A., Fan, X., &
    Noll, K. S. 2009, ApJ, 702, 154
Stetson, P. B. 1987, PASP, 99, 191
Stone, R. C. 1996, PASP, 108, 1051
Tinney, C. G., Burgasser, A. J., & Kirkpatrick, J. D. 2003, AJ,
    126, 975
Tsuji, T. 2005, ApJ, 621, 1033
Vacca, W. D., Cushing, M. C., & Rayner, J. T. 2003, PASP, 115,
    389

Vrba, F. J., Henden, A. A., Luginbuhl, C. B., Guetter, H. H.,
    Munn, J. A., Canzian, B., Burgasser, A. J., Kirkpatrick, J. D.,
    Fan, X., Geballe, T. R., Golimowski, D. A., Knapp, G. R.,
    Leggett, S. K., Schneider, D. P., & Brinkmann, J. 2004, AJ,
    127, 2948